An assessment of fluidized bed dynamics with CPFD simulations

Feichi Zhang[1,*], Salar Tavakkol[1], Lukas Bohlender[1], Stefan Dercho[1], Thorsten Zirwes[2], Michael Zeller[1], Jonas Vogt[1], Dieter Stapf[1]

* feichi.zhang@kit.edu

[1]*Institute for Technical Chemistry, Karlsruhe Institute of Technology (KIT), Herrmann-von-Helmholtz-Platz 1, 76344 Eggenstein-Leopoldshafen*
[2]*Institute for Combustion Technology, University of Stuttgart,Pfaffenwaldring 31, 70569 Stuttgart*

Abstract

The computational particle fluid dynamic (CPFD) method has been used to simulate a laboratory-scale fluidized bed, which has been designed for plastic pyrolysis. The simulations have been performed under cold-mode condition, where only the fluidization of sand particles is considered. The objective of the work is to gain an in-depth understanding of the hydrodynamic behavior of the fluidized bed, which is of particular importance with regard to an efficient mixing and heating of the bed materials as well as the final product yield. The focus of the work is assessing the dynamic behavior of the fluidized bed in terms of the total kinetic energy of all sand particles K_S and the bubble frequency f_B. For validation of the numerical approach, the calculated pressure drop Δp shows good agreement with measured data. In accordance with measurement and theoretical analysis, Δp increases with the bed inventory m_S and remains nearly constant with the bulk gas flow velocity u_G. It has been shown that K_S increases with u_G, which is due to the increased gas flow momentum flux with u_G, leading to a reinforced gas-to-solid momentum exchange. The same behavior has been found for the influence of the sand particle mass m_S on K_S, where K_S increases with m_S. u_G has been found to have a subordinate effect on f_B, whereas f_B decreases with m_S.

An increase in the gas temperature T_G has led to a decreased K_S, while the bed height h_B and Δp remain nearly constant. This is due to the decreased density or momentum flux of the gas flow at higher T_G. While up-scaling the fluidized bed, K_S and f_B have found to be strongly increased, whereas u_G, Δp and h_B were kept constant. The results reveal that it is not sufficient to use solely the general "static" parameters, i.e., h_B and Δp, for characterizing hydrodynamic properties of a fluidized bed. In this case, K_S and f_B represent measures for the available kinetic energy and its fluctuation frequency of the whole fluidized bed system, which are more suitable for assessing the hydrodynamic behavior of the fluidized bed under up-scaled and elevated temperature conditions.

Introduction

Plastics play an important role in our everyday life and is recognized as a key material in construction as well as the medical, automotive, aerospace, electronics and food industries [1]. The global plastics production has increased drastically in the past decades, growing from 1.5 Mt in 1950 to about 390.7 Mt in 2021 [2,3]. The continuing growth in demand for plastics has led to an increased waste accumulation in our living environment. In Europe, about 29.5 Mt of plastics ended up in the waste stream in 2020, about 23% of plastic waste still ends up in landfills, 35% is recycled and 42% is used for energy recovery [3]. Accordingly, energy recovery and landfilling are still the most widely used

methods for treating plastic waste in the EU and worldwide, which lead to severe pollution of soils, drinking water, oceans, and emissions of greenhouse gases.

Currently, the most common way of recycling post-consumer waste plastics is mechanical recycling in which plastic waste is sorted, washed, shredded, melted and extruded, with the actual molecular structure remaining intact [4,5]. This process requires a high purity of the waste feedstock, which limits its application. Moreover, the technical properties of the plastics degrade after each cycle until it can no longer be used for high-quality applications. In addition, not all plastics are compatible with this process.

In order to increase the share of recycled plastics, chemical recycling via pyrolysis has generated increased attention in the last few years due to its advantages in handling contaminated and mixed plastics [6]. During the pyrolysis process, polymer chains of plastics are broken down into a variety of short-chain hydrocarbons in a hot environment without oxygen, which contain a complex blend of molecules and can be further upgraded to basic chemicals or feedstock. The type and composition of the resulting product can be controlled through the reactor design, the operating temperature, pressure and catalysis [7-10]. These process parameters can be adjusted to optimize the process efficiency and product yield. The pyrolysis products can be reused as substitute for fossil feedstock, e.g. to produce new plastics.

The performance of plastic pyrolysis is largely limited by waste feedstock quality and the heating process, as plastics generally have low heat conductivity and are even used as insulation material [11]. Moreover, the pyrolysis reaction is endothermic which hinders the heat transfer from outside to the particle being pyrolyzed. Therefore, the design of a highly efficient heating process is of particular importance for large-scale pyrolysis plants. Fluidized beds have been widely used for engineering applications such as drying, gasification or pyrolysis, due to their advantages with respect to fuel flexibility, low costs, and suitability for continuous production. In particular, the intense mixing of bed materials leads to excellent and homogeneous heating, which is beneficial in terms of plastic pyrolysis. Furthermore, compared with commonly used reactor designs for plastic pyrolysis such as conical spouted bed reactor (CSBR) or tubular reactors, fluidized beds can avoid frequent feeds and clogging phenomena caused by molten plastics. Therefore, the fluidized bed technology is a strong potential solution towards industrial applications of chemical recycling of plastics. Fluidized bed reactors have been used in several recent studies for pyrolysis of plastics [12-15]. Among them, Kaminsky et al. [12] studied the pyrolysis of different plastics with plastic throughput up to 50 kg/h. The results of polyethylene and polypropylene pyrolysis showed a strong temperature dependence. At 400-450°C, the main product is wax, whereas gas and oil are formed at 700°C. Salaudeen [13] et al. studied high-density polyethylene (HDPE) at 500°C. Results showed that wax is the main product. With the addition of olivine, the yield of wax can be increased from 45.6 to 66 wt %. Moreover, the pyro-wax had less branched chains than commercial wax. Tokmurzin [15] investigated the flash pyrolysis of waste plastics in bubbling fluidized beds. As the temperature increased from 600 to 900°C, the gas yield was increased from 0.285 g/g fuel to 0.680 g/g fuel. The preparation method also had an influence on gas yield and fluffy solid recovered fuel (SRF) had a higher gas yield than pelletized SRF.

Despite the achieved progress in the previous works, implementation of the fluidized bed technology for commercial use with a high TRL (technology readiness level) requires detailed knowledge regarding the underlying physio-chemical mechanisms of the whole process. In particular, the operational performance of fluidized beds relies heavily on the hydrodynamics of the gas-solid flow in terms of the formation of bubbles and particle dynamics, which represent the fundamental mechanisms for the mixing or heating process and influence the product yield. However, the harsh environment caused by the dense particulate flow and non-transparent product gas within the fluidized bed limits the experimental assessment of the pyrolysis process. For that reason, 3D, highly-resolved and transient numerical simulations have been conducted for a laboratory-scale fluidized bed reactor, in order to gain insight into the complex hydrodynamic morphologies of the fluidized bed. In addition to the general features such as pressure drop and bed height, the special focus of the work is laid on

evaluating characteristics of the fluidized bed in terms of the total kinetic energy of the sand particles and the bubble frequency, which cannot be assessed from the viewpoint of experiments. The correlations of these properties with the operating parameters have been quantitatively evaluated, which reveals the importance of these parameters on the assessment of the hydrodynamic behavior of fluidized beds.

Simulation methods

- **Multiphase coupling**

As a detailed resolution of each solid particle in the fluidized bed is computationally too expensive, a hybrid Euler-Lagrange method is used in the present work for modeling the multiphase interactions [16]. In this method, the gas flow is regarded as a continuous phase, which is modeled by means of the Naiver-Stokes equations. The solid particles are treated as dispersed, and their trajectories are calculated based on a balance of forces acting on the particles and the equation of motion. Both sets of equations concerning different phases are coupled with each other via individual source terms. For the continuous phase, the following the balance equation for momentum is solved for each computational cell [17]

$$\frac{\partial(\varepsilon\rho_g\boldsymbol{u_g})}{\partial t} + \boldsymbol{\nabla}\cdot(\varepsilon\rho_g\boldsymbol{u_g}\boldsymbol{u_g}) = -\boldsymbol{\nabla}p + \boldsymbol{\nabla}\cdot(\varepsilon\tau_{\text{eff}}) + \varepsilon\rho_g\boldsymbol{g} + \boldsymbol{S_{p,mom}} \tag{1}$$

with the volume fraction of gas ε (also call void fraction or porosity) and the gas density ρ_g; $\boldsymbol{u_g}$ is the gas velocity and $\boldsymbol{g}$ the gravitational acceleration. p is the static pressure and τ_{eff} the effective stress tensor. The momentum exchange between the continuous and disperse phases in Eq.(1) is given by the source term $\boldsymbol{S_{p,mom}}$

$$\boldsymbol{S_{p,mom}} = -\sum_{i=1}^{n_{p,cell}}\frac{\boldsymbol{F_{d,i}}}{V_{cell}} \tag{2}$$

which represents the sum of the drag forces acting on all particles $\boldsymbol{F_{d,i}}$ within the cell volume V_{cell}, with $n_{p,cell}$ being the total number of particles in the current computational cell.

The momentum equation for each discrete particle follows Newton's second axiom [17], where the acceleration of the particles is due to the sum of external forces exerted on the particles

$$m_p\frac{d\boldsymbol{u_p}}{dt} = \sum\boldsymbol{F_{extern}} = \boldsymbol{F_d} + \boldsymbol{F_g} + \boldsymbol{F_c} + \boldsymbol{F_i} \tag{3}$$

The particle positions are then obtained from time integration of the particle velocity $\boldsymbol{u_p}$ with the help of the equation of motion

$$\frac{d\boldsymbol{x_p}}{dt} = \boldsymbol{u_p} \tag{4}$$

In Eq. (3-4), m_p and $\boldsymbol{x_p}$ represent the mass and position vector of the particle; $\boldsymbol{F_c}$ corresponds to the force due to inter-particle collisions; $\boldsymbol{F_g}$ is the result of gravitational and buoyancy forces

$$\boldsymbol{F_g} = m_p\boldsymbol{g}(1 - \frac{\rho_g}{\rho_p}) \tag{5}$$

with the particle density ρ_p. The force $\boldsymbol{F_i}$ is representative for other possible forces that can act on a particle, such as centrifugal or electromagnetic force. $\boldsymbol{F_d}$ is the drag force calculated from the Ergun-Wen-Yu model [17, 18]:

$$\boldsymbol{F_d} = \begin{cases} \dfrac{m_p}{\rho_p}\left(150\dfrac{1-\varepsilon}{\varepsilon} + 1.75Re\right)\dfrac{\mu_g|\boldsymbol{u_g} - \boldsymbol{u_p}|}{\varepsilon\sqrt{d_p}}, & \varepsilon < 0.8 \\[4mm] \dfrac{m_p}{\rho_p}0.75\cdot C_dRe\dfrac{\mu_g\varepsilon^{-2.65}|\boldsymbol{u_g} - \boldsymbol{u_p}|}{\varepsilon\sqrt{d_p}}, & \varepsilon \geq 0.8 \end{cases} \tag{6}$$

with the particle diameter d_p, the Reynolds number Re and the gas phase viscosity μ_g. The drag coefficient C_d is calculated as a function of Re and ε.

$$C_d = \begin{cases} 24\cdot(1 + 0.15\cdot(\varepsilon\cdot Re)^{0.687}, & Re \leq 1000 \\ 0.44\cdot\varepsilon\cdot Re, & Re > 1000 \end{cases} \tag{7}$$

3

- **Modeling of inter-particle collisions**

As the Discrete Element Method (DEM) or the Discrete Particle Method (DPM) for modeling the inter-particular force is computationally too expensive due to the evaluation of the collisional force based on contact detections of the individual particles [19], the Multiphase Particle in Cell (MP-PIC) method has been used to model the particle collisions. In addition, the MP-PIC method uses the parcel concept, where each parcel represents a collective of a number of particles with the same size and velocity [20]. The collision force between the particles is given by

$$\boldsymbol{F}_c = -\frac{m_p}{\alpha_p \rho_p} \nabla \tau_p \qquad (8)$$

$$\tau_p = \frac{p_s \alpha_p^\beta}{\max\{(\epsilon \cdot \varepsilon),(\alpha_{packed} - \alpha_p)\}} \qquad (9)$$

The particle stress τ_p is calculated according to the modified Harris-Crighton model [21, 22], where p_S, is the normal particle stress, β an empirical exponent and α_{packed} corresponds to the particle close pack volume fraction at the densest packing. In the current work, these parameters are set to $p_s = 10$ N/m^2, $\beta = 2$ and $\alpha_{\text{packed}} = 0.65$. A small value for ϵ is used to avoid division by zero, i.e., $\epsilon = 10^{-7}$. The off-center particle collisions result in scattering of the particles in all spatial directions. This effect has been considered by an isotropy model, which corrects the flow velocity of the particle based on a stochastic process [23].

The particle-wall collision is modelled with the rebound model, where the velocity of each particle after collision with a wall is calculated from the following equation

$$\begin{pmatrix} u_{new,t} \\ u_{new,n} \end{pmatrix} = \begin{pmatrix} u_{old,t} \\ u_{old,n} \end{pmatrix} - (1+e) \begin{pmatrix} 0 \\ u_{old,n} \end{pmatrix} - \mu \begin{pmatrix} u_{old,t} \\ 0 \end{pmatrix} \qquad (10)$$

where $(u_{new,t}, u_{new,n})$ are the newly calculated particle velocities in the tangential and normal direction with respect to the wall. $(u_{old,t}, u_{old,n})$ are the particle velocities before the collision; e is the coefficient of elasticity for the normal direction to the wall and indicates elasticity of the impact. For $e = 1$ the impact is fully elastic and for $e = 0$ the impact is plastic. The same applies to the restitution coefficient μ, where $\mu = 0$ indicates a fully elastic and $\mu = 1$ a fully plastic impact.

Simulation Setups

The simulations have been conducted for a generic, laboratory-scale fluidized bed designed for studying the pyrolysis process of plastics. The geometry is given by a cylindrical quartz glass, having a diameter of 5 cm and a length of 60 cm. Silica sand particles have been used as carrier material, which are fluidized with nitrogen as fluidizing agent. The gas passes through a sintered metal plate located at the ground of the tube, which leads to a homogeneous inflow over the entire ground area. The fluidized bed is operated at atmospheric conditions at 1 atm and 25°C. The bulk gas flow velocity u_G has been varied from 14 to 29 cm/s and the sand inventory m_S from 195 to 586 g, as shown in Tab.1. In addition, an increased gas temperature at 500°C has been used to study the fluidization behavior under hot conditions. Moreover, in order to study the effect of up-scaled reactor dimensions, the reactor radius has been varied from $d_R = 3$ cm up to $d_R = 10\ cm$. The experiments as well as the simulations have been conducted in a cold-mode condition without considering the plastic particles and the pyrolysis reaction. In this case, focus of the study has been laid on the correlations of hydrodynamic behavior of the fluidized bed with varied operating parameters.

Table 1: Operating parameters used for the simulations of the laboratory-scale fluidized bed.

m_S [g]	195	293	390	488	586
u_G [cm/s]	13.6	16.9	21.2	25.4	29.7

The simulation domain is given by a cylinder with the same geometrical dimensions as used in the experiments. The gas inlet is located at the exit plane of the sintered metal. The computational grid consists of approx. 150,000 hexahedral elements, using an almost equidistant resolution of 1 mm. Four million parcels have been used to render the sand particles. The number of particles per parcel increases with the sand mass, ranging from 3 to 8. A Gaussian normal distribution and a mean diameter of 0.213

mm has been used to reproduce the measured size distribution of sand particles. The non-slip condition has been used for the gas velocity on the reactor wall. The velocity at the inlet is set to $u_{G,0}/\varepsilon$, with $u_{g,0}$ being the bulk flow velocity and ε the void fraction or the volume fraction of the continuous phase, respectively. At the outlet of the reactor, the gradient of the gas velocity is set to zero. The sand particles have been introduced from given locations distributed along the whole reactor and with an initial velocity of 0 m/s, which fall to the ground of the reactor at the beginning and build a fluidized bed over time due to the interactions with the gas flow.

The open-source CFD code OpenFOAM-v2112 has been used to perform the simulations, employing the standard solver MPPICFoam available in OpenFOAM. The balance equations for the continuous phase are solved in an incompressible formulation under isothermal conditions, along with 1st and 2nd order interpolation schemes for discretization of the convective and diffusive terms. The time step is set to 0.1 ms, which leads to a maximum CFL (Courant-Friedrichs-Lewy) below unity. The gas flow is treated as laminar, as the inflow velocity or the Reynolds number is low (Re<1000). The initial flow velocity is set to 0 for the whole computational domain. The simulations have been run for a physical time of 8 s and with 128 processors (1 node) from the HAWK cluster at the High-Performance Computing Center Stuttgart (HLRS).

Results

- **Morphology of the fluidized bed**

Figure 1 depicts time series of the contours of calculated void or gas fraction ε on a cutting plane passing the centerline axis for the case with $m_S = 293$ g and $u_G = 0.21$ m/s, where the black dots indicate the sand particles. Only a small portion (ca. 1%) of the totally simulated Lagrange parcels are shown and they are scaled up by a factor of 5 for better visualization. The time intervals between each snapshots is given by ¼ of the bubbling period. The bubbles can be detected by the red zones with large ε. Although not shown here, the morphology of the fluidized bed reveals a bubbling fluidization regime for all considered cases, which is in accordance with the experiments and the preliminary design. While the gas flow passes through the sand bed, small bubbles are first generated in the lower part of the reactor and rise along the reactor axis due to the buoyancy force. With increased axial distance, the size of bubbles increases due to the coalescence of small bubbles. The motion of the bubbles leads to an intense mixing of sand particles. The hydrodynamic behavior in the current case is dominated by a large bubble, which is due to the use of a relatively small reactor dimension at $d_R = 5$ cm.
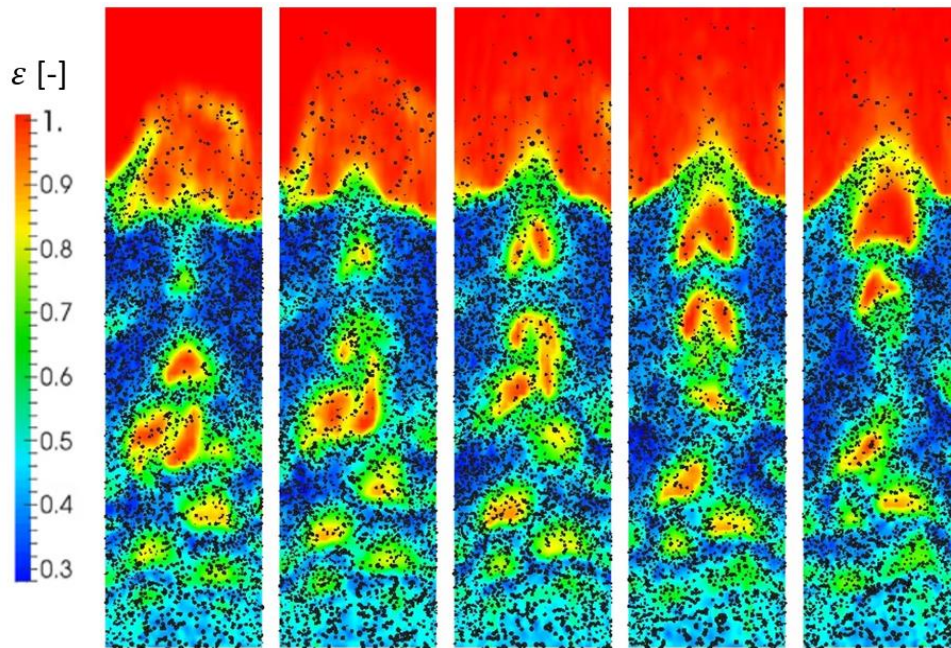
Figure 1: Instantaneous contours of void fraction for the case with $m_S = 293$ g, $u_G = 0.21$ m/s on a cutting plane passing through the centerline axis.

In Fig.2, the pressure drop Δp evaluated from simulations and experiments are compared with each other, which show a reasonably good agreement for different operating conditions. Δp remains almost constant with u_G. However, Δp increases strongly with m_S, which is due to the increased flow resistance with m_S. The calculated Δp is underestimated compared with the measured data, which could be due to the assumptions of the MP-PIC approach and wall collision model used in this work, which lead to an underestimation of energy loss during the multiphase interactions. The effect is of particular importance for the current relatively small reactors, where the interactions of particle and gas flow with the reactor wall dominates the underlying flow pattern. In addition, the discrepancy between experiment and simulation is larger for increased m_S.
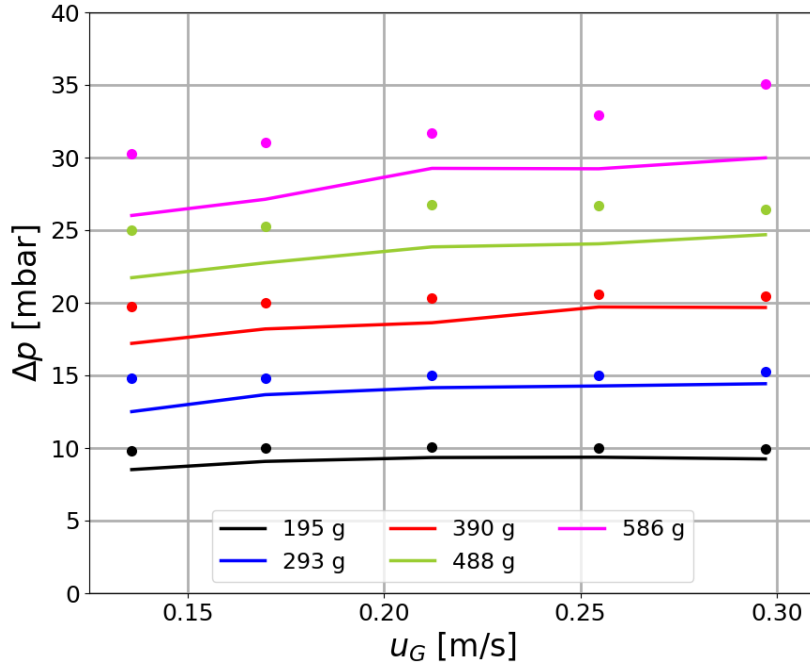
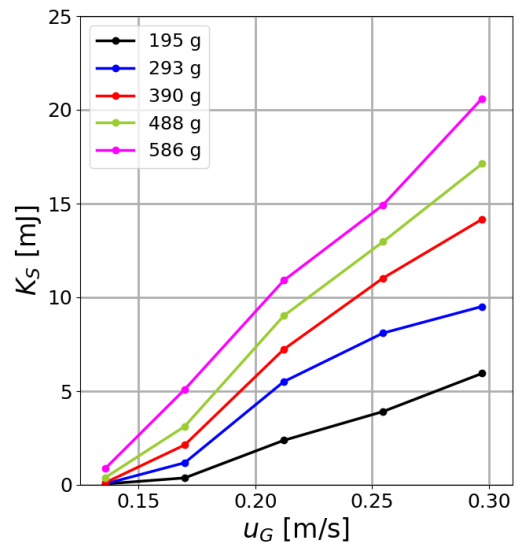**Figure 2:** Comparison of calculated (lines) and measured (dots) pressure drop.

The fluidization process is prevailed by the chaotic motion of the gas bubbles and sand particles, which correlate strongly with the operating parameters. In order to access the hydrodynamic behavior of the fluidized bed, the overall kinetic energy in the fluidized bed K_S has been evaluated by summing up the kinetic energies of each sand particle

$$K_S = \frac{1}{2}\sum_{i=1}^{N_p} m_{p,i} u_{p,i}^2$$

with the mass and velocity of each sand particle $m_{p,i}$ and $u_{p,i}$. Note that K_S represents an integral parameter, which measures the total kinetic energy of all sand particles available in the fluidized bed. Figure 3 depicts the time-averaged value of K_S, which increases with u_G. This is attributed to the increased momentum flux of the gas phase or the reinforced momentum transfer from the gas to the solid phase. In addition, K_S increases with m_S due to the increased mass of bed inventory.

Figure 3: Correlation of total kinetic energy of sand particles with inflow gas velocity at different sand masses.
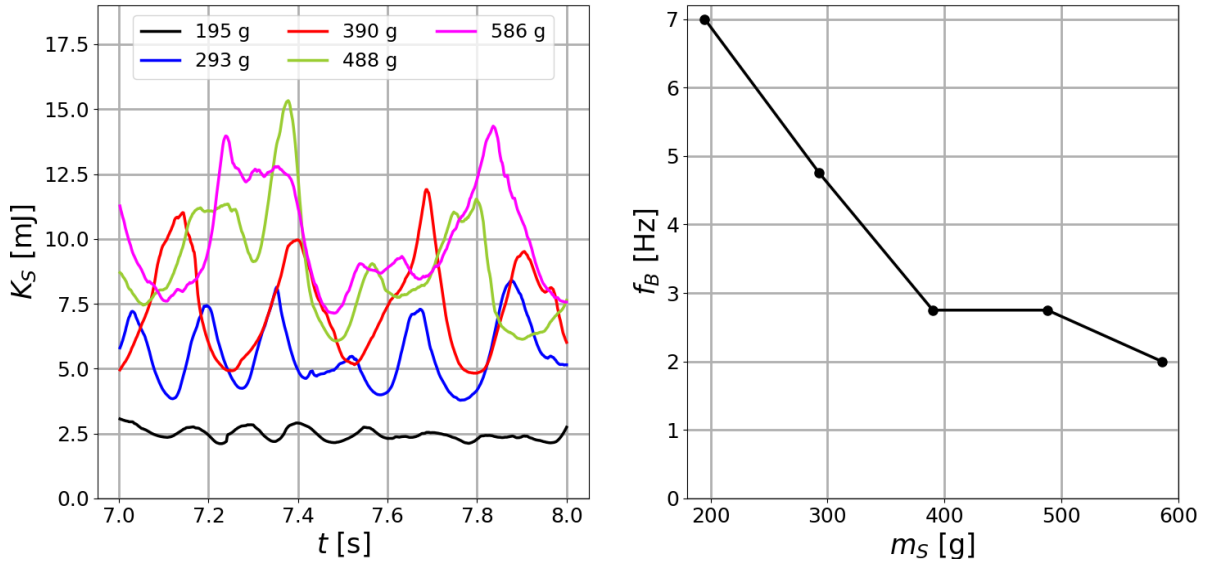
- **Bubble frequency**

The periodically rising bubbles and the bursting of these bubbles at the upper surface of the bed trigger the whole bed system into a pulsating mode with distinct frequencies. This bubble frequency f_B

6

corresponds to the number of repetitions of the recurring bubbles within one second and represents a measure for the moving speed or dynamics of the rising bubbles. This quantity has been evaluated in this work from spectral analysis (Fourier transformation) of the temporal development of K_S. In Fig. 4, the diagram on the left shows the calculated time progress of K_S for a constant gas velocity $u_G = 0.21$ m/s and different sand mass m_S, which exhibit distinct periodical fluctuations. The time mean value and the fluctuation amplitude of K_S increase with m_S, as shown in Fig.3 and Fig.4 on the left, which is due to the increased total mass of sand particles. In addition, the number of repetitions of K_S decreases with m_S, indicating a decrease of the bubble frequency f_B with m_S, as shown in Fig.4 on the right. The reason is attributed to the fact that the bed height h_{FB} is increased with m_S, which leads to a longer rising distance from the bottom to the top of the reactor or the increased residence time of the bubble, respectively.

Figure 4: Time development of kinetic energy of sand particles (left) and dependency of bubble frequency of the fluidized bed with sand mass (right).

In the case of m_S=195 g, the fluidized bed is short and dominated by solely small bubbles, which do not have sufficient time to coalesce to large bubbles before reaching the upper surface of the fluidized bed. Therefore, f_B is at its largest in this case. With increased m_S, the fluidized sand bed expands and the bubbles have more space to coalesce, so that fewer bubbles with large diameters reach the surface of the fluidized bed. This results in a decreased f_B with m_S. Moreover, the temporal progress of K_S does not show a harmonic or sinusoidal behavior, which is caused by the mutual interactions between the simultaneously rising and bursting bubbles. Although not shown here, u_G was found to have a subordinate influence on f_B, which corresponds to the correlations of the pressure drop (see Fig.2) and the bed height with u_G.

- **Effect of gas temperature**

Plastics pyrolysis takes place generally in a high-temperature environment. In order to study the effect of operating temperature on the hydrodynamic behavior of the fluidized bed, an additional simulation has been carried out for an elevated gas temperature with $T_G = 500°C$. The sand mass and gas velocity have been kept constant at $m_S = 293$ g and $u_G = 0.21$ m/s. However, the density of the gas is decreased from $\rho_G = 1.14$ kg/m^3 to $\rho_G = 0.44$ kg/m^3 while varying T_G from 20°C to 500°C, which results in a decreased momentum flux of the gas flow.

The left part of Fig.5 compares the instantaneous contours of the void fraction ε on a meridian cutting plane passing through the symmetry axis. As m_S and u_G are kept constant while varying T_G, the bubbling fluidization regime as well as the bed height remain almost unchanged at different T_G. However, the high-temperature condition results in a delayed formation of bubbles at the bottom of the fluidized bed, as indicated by the ellipsis shown in Fig.4 on the left. This is attributed to the fact that the momentum flux of the gas flow decreases with T_G due to the decreased gas density. The same behavior can be detected from the time-mean contours of ε shown in the middle of Fig.5, where ε near the base of the reactor is smaller for the case with $T_G = 500°C$ compared with that at ambient temperature.

The diagram on the right of Fig.5 shows that the kinetic energy of sand K_S is decreased by more than 50 % while increasing T_G from 20°C to 500°C. The reason is attributed to the decreased momentum flux or density of the gas flow with T_G, leading to a weakened momentum exchange from the gas to the solid phase. In addition, the bubble frequency remains almost constant with increased T_G, which can be detected from the time evolution of K_S shown on the right of Fig.5. Although not presented here, the pressure drop remains almost constant with increased T_G, too.
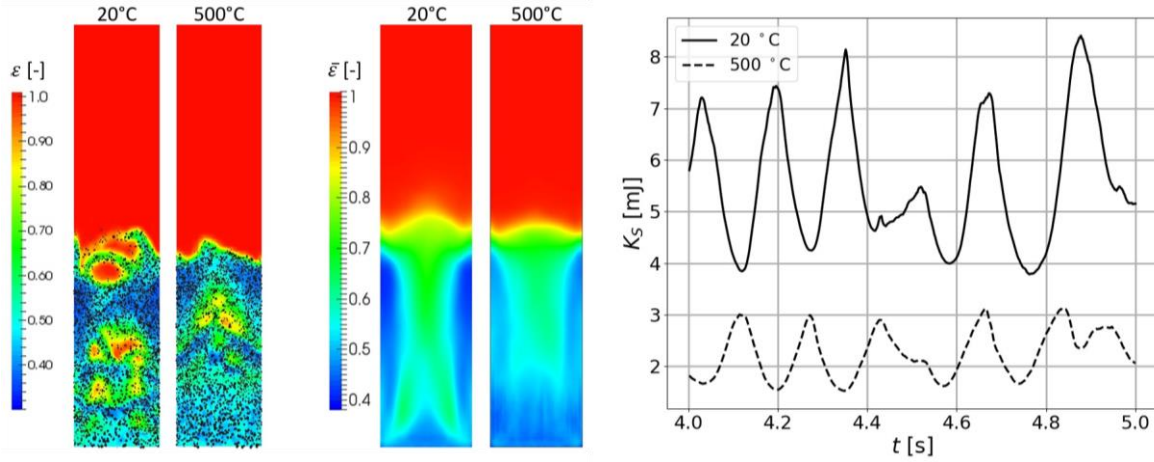
Figure 5: Comparison of instantaneous (left) and time mean contours of porosity (middle), and time evolution of kinetic energy of sand particles at the gas temperatures of $T_G = 20°C$ and $T_G = 500°C$ (right).

- **Effect of up-scaling**

In order to study the effect of up-scaled fluidized beds on the hydrodynamic properties, an approach with constant pressure drop and bed height has been chosen, while the same gas velocity with $u_G = 0.21$ m/s and particle sizes are used. In this way, the bed inventory yields a quadratic increase with the reactor diameter d_R ($m_S \propto d_R^2$), whereas the bubbling fluidization regime remains unchanged. For the numerical simulation, the grid resolution has been kept constant at $\Delta \approx 1$ mm for up-scaled reactors, which leads to an increased overall cell number with reactor size.
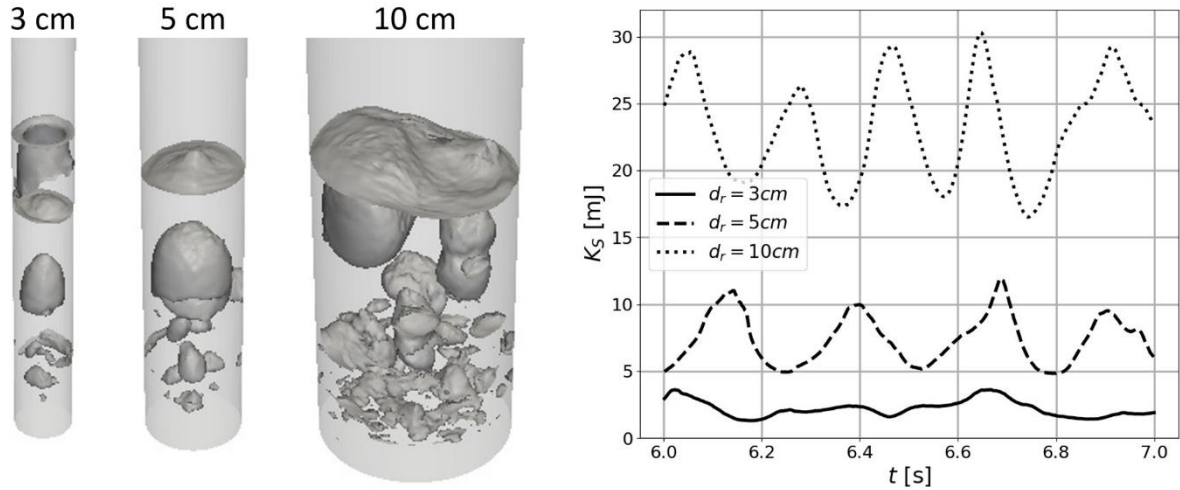
Figure 6: Comparison of bubble formation in up-scaled reactors (left) and temporal development of kinetic energy of sand particles for up-scaled fluidized beds (right).

The left-hand side of Fig.6 depicts snapshots of iso-contours of $\varepsilon = 0.66$ for different reactor sizes ranging from $d_R = 3$ cm to $d_R = 10$ cm, which illustrate geometrical structures of the formed bubbles. For the small reactors with $d_R = 3$ cm and $d_R = 5$ cm, the hydrodynamic behavior is dominated by a single large bubble rising along the centerline axis. This is attributed to the narrow margin bounded by the reactor wall, which slows down the gas flow due to the non-slip condition and leads to an intensive coalescence of small bubbles. However, in the case of $d_R = 10$ cm, the number of bubbles is increased

significantly, where the bubbles rise along multiple columns. The enhanced formation of bubbles as well as the increased sand mass lead to an increased kinetic energy of sand particles K_S with d_R, as illustrated in Fig.6 on the right, showing the temporal development of K_S for different reactor sizes. Both the time mean value of K_S as well as its fluctuation amplitude are increased strongly with the degree of up-scaling. In addition, the up-scaled reactor leads to an increase of the bubble frequency f_B, which can be identified from the increased number of periodical repetitions of K_S within 1s in Fig.6 on the right. This is attributed to the fact that the bursting of the bubbles happens more frequently due to the reinforced formation of bubbles.

Conclusion

A laboratory-scale fluidized bed reactor developed for the pyrolysis of plastic waste has been studied numerically in cold-mode operation. The objective of the work is to assess the hydrodynamic behavior of the fluidized bed in terms of the total kinetic energy of all sand particles K_S and the bubble frequency f_B. The bubbling fluidization regime of the fluidized bed observed in experiments has been reproduced well by the simulations, where the calculated pressure drop Δp has shown a good agreement with measured data.

An increased bulk flow velocity of the gas u_G has led to an increased K_S due to the enhanced multiphase momentum exchange, which is attributed to the increased momentum flux of the gas flow. The same behavior has been found for the effect of the bed inventory m_S on K_S. In addition, f_B decreases with m_S due to the increased bed height h_B or rising distance of the bubble along the reactor. On the contrary, the effects of u_G on f_B and h_B have been confirmed to be subordinate.

While keeping Δp and h_B constant at given m_S and u_G, K_S has been found to decrease with increased gas temperature T_G due to the decreased density or momentum flux of the gas flow. By increasing the bed inventory via up-scaling at the same time as the reactor dimension, K_S and f_B are increased significantly, while Δp and h_B remain constant. The results reveal distinct correlations between the dynamic parameters, i.e., K_S and f_B, with the operating parameters, which can be used to characterize the hydrodynamic behavior of the fluidized bed. In particular, this work indicates that the commonly used "static" properties such as Δp and h_B are not sufficient for studying scale-up or temperature effects, as these remain unchanged under up-scaled or elevated temperature conditions. Therefore, the proposed dynamic properties represent suitable measures for a detailed assessment of the overall behavior of fluidized beds in plastics pyrolysis, where proper mixing and heat-up of meltable plastics particles is crucial for process control and reliability.

Acknowledgments

References

[1]   Al-Salem S. M., Antelava A., Constantinou A., Manos G., Dutta A.: *A review on thermal and catalytic pyrolysis of plastic solid waste (PSW)*, Journal of environmental management, 197, 177-198, 2017.

[2]   Shanmugam V., Das O., Neisiany R. E., Babu K., Singh S., Hedenqvist M. S., Berto F., Ramakrishna S.: *Polymer Recycling in Additive Manufacturing: an Opportunity for the Circular Economy*, Materials Circular Economy, 2, 11, 2020.

[3]   Plastics Europe: *Plastics - the Facts 2022*. https://plasticseurope.org/knowledge-hub/plastics-the-facts-2022/, 2022

[4]   Rahimi A., García J. M.: *Chemical recycling of waste plastics for new materials production,* Nature Reviews Chemistry, 1, 0046, 2017.

[5] Li H., Aguirre-Villegas H. A., Allen R. D., Bai X., Benson C. H., Beckham G. T., Bradshaw S. L., Brown J. L., Brown R. C., Cecon V. S., Curley J. B., Curtzwiler G. W., Dong S., Gaddameedi S., García J. E., Hermans I., Kim M. S., Ma J., Mark L. O., Mavrikakis M., Olafasakin O. O., Osswald T. A., Papanikolaou K. G., Radhakrishnan H., Sanchez Castillo M. A., Sánchez-Rivera K. L., Tumu K. N.: *Expanding plastics recycling technologies: chemical aspects, technology status and challenges*, Green Chemistry, 24, 8899-9002, 2022.

[6] S. Q. Muhammad, Oasmaa A., Pihkola H., Deviatkin I., Tenhunen A., Mannila J., Minkkinen H., Pohjakallio M., Laine-Ylijoki J.: *Pyrolysis of plastic waste: Opportunities and challenges*, Journal of Analytical and Applied Pyrolysis, 152, 104804, 2020.

[7] Schubert T., Lechleitner A., Lehner M., Hofer W.: *4-Lump kinetic model of the co-pyrolysis of LDPE and a heavy petroleum fraction*, Fuel, 262, 116597, 2020.

[8] Mastellone M. L., Arena U.: *Fluidized-bed pyrolysis of polyolefins wastes: Predictive defluidization model*, AIChE journal, 48(7), 1439-1447, 2004.

[9] Kunwar B., Cheng H. N., Chandrashekaran S. R., Sharma B. K.: *Plastics to fuel: a review*, Renewable and Sustainable Energy Reviews, 54, 421-428, 2016.

[10] Goto M.: *Chemical recycling of plastics using sub-and supercritical fluids*, The Journal of Supercritical Fluids, 47(3), 500-507, 2009.

[11] Radhakrishnan K., Kumar P.S., Rangasamy G., Perumal L. P., Sanaulla S., Nilavendhan S., Manivasagan V., Saranya K.: *A critical review on pyrolysis method as sustainable conversion of waste plastics into fuels*, Fuel, 337, 126890, 2023.

[12] Kaminsky W.: *Chemical recycling of plastics by fluidized bed pyrolysis*, Fuel Communications, 8, 100023, 2021.

[13] Salaudeen S. A., Al-Salem S. M., Sharma S., Dutt A.: *Pyrolysis of High-Density Polyethylene in a Fluidized Bed Reactor: Pyro-Wax and Gas Analysis*, Ind. Eng. Chem. Res., 60, 18283−18292, 2021.

[14] Al-Salem S. M., Haute M. V., Karam H. J., Hakeem A., Meuldermans W., Patel J., Hafeez S., Manos G., Constantinou A.: *Fuel Range Properties of Oil and Wax Obtained from Catalytic Pyrolysis of Linear Low-Density Polyethylene in a Fluidized Bed Reactor (FBR)*, Ind. Eng. Chem. Res., 61, 43, 16383–16392, 2022.

[15] Tokmurzin D., Nam J. Y., Lee T. R., Park S. J., Nam H., Yoon S. J., Mun T., Yoon S. M., Moon J. H., Lee J. G., Lee D. H., Ra H.W., Seo M. W.: *High temperature flash pyrolysis characteristics of waste plastics (SRF) in a bubbling fluidized bed: Effect of temperature and pelletizing*, Fuel, 326, 125022, 2022.

[16] Kuerten M. J. G.: *Point-Particle DNS and LES of Particle-Laden Turbulent flow - a state-of-the-art review*, Flow Turbulence Combust, 97, 689–713, 2016.

[17] Alobaid F., Almohammed N., Farid M. M., May J., Rößger P., Richter A., Epple B.: *Progress in CFD Simulations of Fluidized Beds for Chemical and Energy Process Engineering*, Progress in Energy and Combustion Science, 91, 100930, 2022.

[18] Gidaspow, D.: *Multiphase Aow and Auidization: Continuum and kinetic theory description*, Academic Press, San Diego, ISBN: 9780122824708, 1994.

[19] Loha C., Gu S., De Wilde J., Mahanta P., Chatterjee P. K.: *Advances in mathematical modeling of fluidized bed gasification*, Renewable and Sustainable Energy Reviews, 40, 688-715, 2014.

[20] Snider D. M., O`Rourke P. J., Andrews M. J.: *An incompressible two-dimensional multiphase particle-in-cell model for dense particle flows*, United States: N. p., 1997.

[21] Harris S. E., Crighton D. G.: *Solutions, solitary waves and voidage disturbances in gas-fluidized beds*, J. Fluid Mech., 266, 243, 1994.

[22] Snider D. M.: *An Incompressible Three-Dimensional Multiphase Particle-in-Cell Model for Dense Particle Flows*, Journal of Computational Physics, 170, 2, 523-549, 2001.

[23] O'Rourke P. J., Snider D. M.: *Inclusion of collisional return-to-isotropy in the MP-PIC method*, Chemical Engineering Science, 80, 39-54, 2012.